Interfacial-engineering-enabled practical low-temperature sodium metal battery

Tao Deng[1,2,6], Xiao Ji[1,6], Lianfeng Zou[3], Obinna Chiekezi[4], Longsheng Cao[1], Xiulin Fan[1], Toyosi R. Adebisi[4], Hee-Jung Chang[2], Hui Wang[2], Bin Li[5], Xiaolin Li[2], Chongmin Wang[3], David Reed[2], Ji-Guang Zhang[2], Vincent L. Sprenkle[2], Chunsheng Wang[1✉] and Xiaochuan Lu[4✉]

Solid-state sodium (Na) batteries have received extensive attention as a promising alternative to room-temperature liquid electrolyte Na-ion batteries and high-temperature liquid electrode Na–S batteries because of safety concerns. However, the major issues for solid-state Na batteries are a high interfacial resistance between solid electrolytes and electrodes, and Na dendrite growth. Here we report that a yttria-stabilized zirconia (YSZ)-enhanced beta-alumina solid electrolyte (YSZ@BASE) has an extremely low interface impedance of $3.6\,\Omega\,cm^2$ with the Na metal anode at 80 °C, and also exhibits an extremely high critical current density of ~7.0 mA cm^{-2} compared with those of other Li- and Na-ion solid electrolytes reported so far. With a trace amount of eutectic NaFSI–KFSI molten salt at the electrolyte/cathode interface, a quasi-solid-state Na/YSZ@BASE/NaNi$_{0.45}$Cu$_{0.05}$Mn$_{0.4}$Ti$_{0.1}$O$_2$ full cell achieves a high capacity of 110 mAh g^{-1} with a Coulombic efficiency >99.99% and retains 73% of the cell capacity over 500 cycles at 4C and 80 °C. Extensive characterizations and theoretical calculations prove that the stable β-NaAlO$_2$-rich solid–electrolyte interphase and strong YSZ support matrix play a critical role in suppressing the Na dendrite as they maintain robust interfacial contacts, lower electronic conduction and prevent the continual reduction of BASE through oxygen-ion compensation.

Sodium (Na)-ion/metal batteries have been recognized as one of the most promising alternatives to Li-ion batteries for renewable energy market because Na has properties similar to those of Li but costs less[1–3]. Compared with liquid electrolyte Na-ion batteries, solid-state Na batteries (SSNBs) can simultaneously achieve a high energy/power density and excellent safety, and thus reduce the manufacturing and/or maintenance costs[4,5]. All of these make SSNBs ideal power sources for renewable energy applications.

The solid-state electrolyte (SSE) is a critical component for SSNBs. The ideal SSE should have a high Na-ion conductivity (that is, $\sigma_{Na} \geq 10^{-4}\,S\,cm^{-1}$), negligible electronic conductivity, excellent compatibility with electrodes, remarkable Na dendrite suppression capability, wide electrochemical stability window and satisfactory mechanical strength at a lower operating temperature (preferably at room temperature (RT))[6–8]. Currently, there are no electrolytes that can satisfy all these requirements even though Na superionic conductors[4,6], sulfide-based solid electrolytes (for example, Na$_3$PS$_4$ (ref. [9]), xNa$_2$S$(100-x)$P$_2$S$_5$ (ref. [10]) and Na$_3$SbS$_4$ (ref. [11]), and beta-alumina (β″-Al$_2$O$_3$) solid electrolytes (BASEs) have been extensively investigated.

Among all the Na-ion conducting SSEs, BASEs have high ionic conductivities (~1×10^{-3} and ~0.2 S cm^{-1} at RT and 300 °C, respectively), negligible electronic conductivity and excellent compatibility and/or chemical stability with electrode materials[12–14]. Currently, BASE membranes are used in high-temperature (280–350 °C) sodium–sulfur (Na–S) and sodium–metal halide (ZEBRA) batteries[15–18]. The high temperature increases the manufacturing and/or maintenance costs, leads to performance degradation and causes

safety concerns[5,19–21]. Reducing the temperature below the melting point of Na metal would suppress these issues. However, it brings another problem, a significant increase in BASE/electrode interfacial resistance, which tends to incur Na dendrite formation. Recent advances demonstrated that an increase of stacking pressure and temperature can dramatically reduce the interfacial resistance and increase the critical current density (CCD) for Li/Na-ion SSEs (Supplementary Table 1). For example, Battaglia and co-workers achieved an average CCD of 19 mA cm^{-2} at 60 °C with a pressure of 3.4 MPa and a limiting capacity of 0.25 mAh cm^{-2} (ref. [22]). Overall, the interfacial stability of BASE/Na needs to be improved for Na metal batteries to operate under realistic conditions (for example, a thin electrolyte and mild temperature and/or stacking pressure), which is currently extremely challenging.

Here we incorporated ~37 wt% yttria-stabilized zirconia to BASE (YSZ@BASE), which reduced the interfacial resistance from 6.6 (BASE/Na) to $3.6\,\Omega\,cm^2$ (YSZ@BASE/Na) at 80 °C, and the low interfacial resistance was maintained during >330 hours of cycling. CCD of the YSZ@BASE in symmetric Na/YSZ@BASE/Na cells reached a very high value of ~7.0 mA cm^{-2} under a mild pressure of ~0.18 MPa at 80 °C, which is nearly five times that of the pure BASE without YSZ (~1.5 mA cm^{-2}). Full cells with a Ni-rich cathode achieve a high initial capacity of 110 mAh g^{-1} and maintain 73% of the capacity over 500 cycles with a coulombic efficiency >99.99% at a rate of 4 C. This study represents a new class of sodium batteries with a significantly lower operating temperature and a higher safety than those of the state-of-the-art Na–S, ZEBRA and other solid-state batteries.

¹Department of Chemical and Biomolecular Engineering, University of Maryland, College Park, MD, USA. ²Energy and Environment Directorate, Pacific Northwest National Laboratory, Richland, WA, USA. ³Environmental Molecular Sciences Laboratory, Pacific Northwest National Laboratory, Richland, WA, USA. ⁴Department of Applied Engineering Technology, North Carolina A&T State University, Greensboro, NC, USA. ⁵Energy Storage & Advanced Transportation Department, Idaho National Laboratory, Idaho Falls, ID, USA. ⁶These authors contributed equally: Tao Deng, Xiao Ji. ✉e-mail: cswang@umd.edu; xlu@ncat.edu
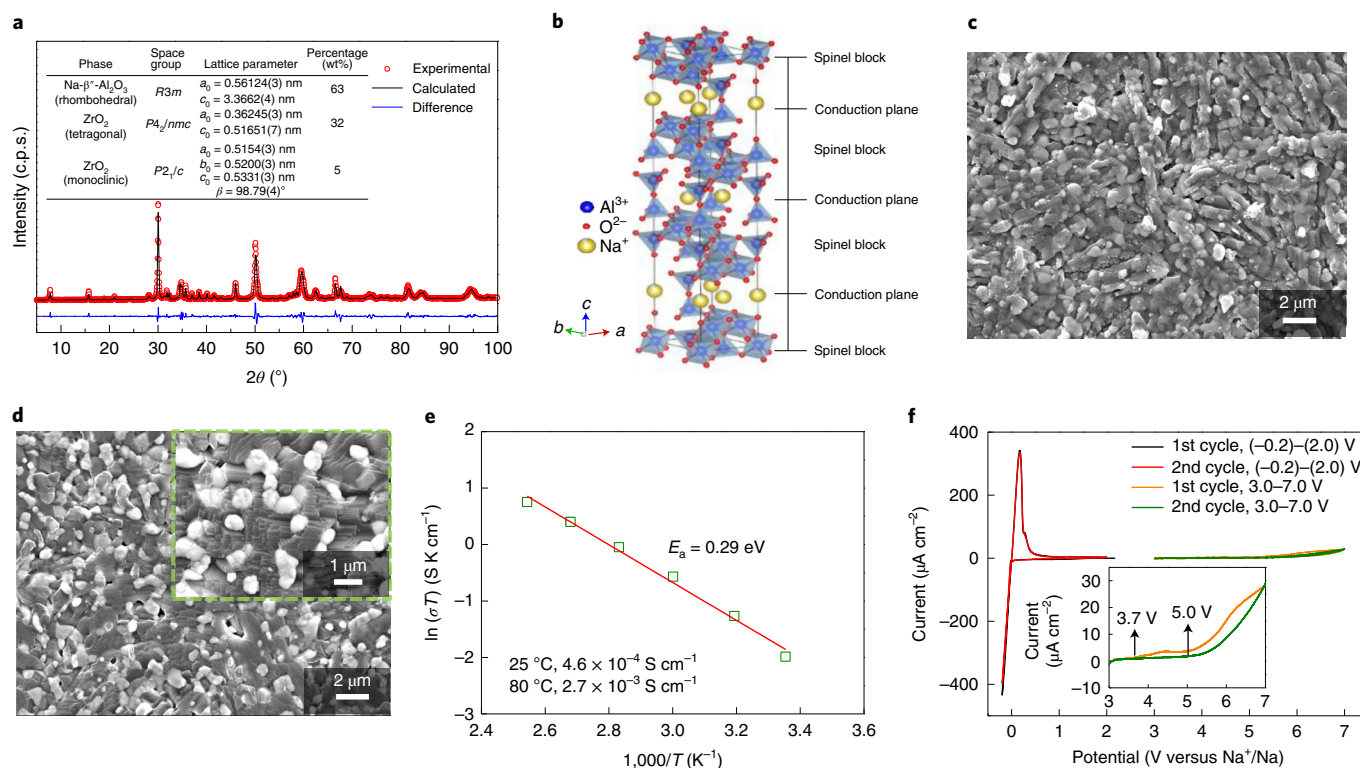
Fig. 1 | Characterization of YSZ@BASE. a, Rietveld refinement results of powder XRD of a YSZ@BASE sample. **b**, Schematic of the idealized structure of BASE, which consists of conduction planes and spinel blocks. **c,d**, SEM images of the YSZ@BASE sample at the surface (**c**) and in a cross-section (**d**). **e**, Arrhenius plot of the conductivity of the YSZ@BASE sample at different temperatures. E_a, activation energy. **f**, CV of a Na/YSZ@BASE/Au blocking electrode cell within −0.2–2.0 V (0.3 mV s^{-1}). Inset: Na/YSZ@BASE/YSZ@BASE–C/Au semiblocking electrode cell within 3.0–7.0 V (0.05 mV s^{-1}) at RT. c.p.s., counts per second.

Results and discussion

Characterization of YSZ@BASE. The YSZ@BASE with an excellent mechanical strength (Supplementary Fig. 1) was fabricated via a vapour-phase conversion process, as described in our previous works[12,13]. The structural parameters and composition of the YSZ@BASE powder were obtained by X-ray diffraction (XRD) refined with the Rietveld method (Fig. 1a and Supplementary Fig. 2). The YSZ@BASE consists of β″-Al$_2$O$_3$ (63 wt%), tetragonal ZrO$_2$ (32 wt%) and monoclinic ZrO$_2$ (5 wt%). The addition of YSZ does not change the crystal structure of β″-Al$_2$O$_3$.

The structure of β″-Al$_2$O$_3$ consists of alternating closely packed spinel blocks and loosely packed conduction planes (Fig. 1b). The conduction planes contain a high concentration of Na$^+$, which are free to move within the planes perpendicular to the c axis under an electric field[18]. Scanning electron microscopy (SEM) images of the sample indicate that submicrometre spherical YSZ particles (white) are uniformly distributed in the rod-shaped β″-Al$_2$O$_3$ matrix (grey) on the surface (Fig. 1c), which is more obvious in the cross-sectional image after polishing and thermal etching (Fig. 1d). The even distribution of the YSZ and BASE phases was further confirmed by energy-dispersive X-ray spectroscopy (EDS) mapping of O, Na, Al, Y and Zr elements (Supplementary Figs. 3 and 4). In comparison, the pure BASE shows a similar microstructure with granular β″-Al$_2$O$_3$ particles (Supplementary Fig. 5a). The relative density of both samples measured by the Archimedes method was above 98%. Based on electrochemical impedance spectroscopy (EIS) and the corresponding fitting results (Fig. 1e and Supplementary Fig. 6), the total (bulk + grain boundary) conductivity of the YSZ@BASE was 4.6×10^{-4} S cm^{-1} at RT and increased to 2.7×10^{-3} S cm^{-1} at 80 °C. The conductivity of YSZ@BASE at RT is nearly half that of pure BASE (1.1×10^{-3} S cm^{-1}; Supplementary Fig. 5b) due to the existence of ~37 wt% YSZ in the former.

The cyclic voltammetry (CV) curve in Fig. 1f shows a highly reversible Na plating/stripping at −0.2 and 0.16 V. The electrolyte also shows a high anti-oxidation capability, as evidenced by an undetectable anodic current until 3.7 V (versus Na/Na$^+$), and the kinetic limit for oxidation can be as high as 5.0 V (versus Na/Na$^+$) after forming a passivating film[23]. X-ray photoelectron spectroscopy (XPS) analysis (Supplementary Fig. 7) revealed that moisture and CO$_2$ in the air can react with the BASE phase to form a thick surface passivation layer that consisted of Na$_2$CO$_3$, Al(OH)$_x$, NaOH and so on. This passivation layer tends to increase the surface resistance with Na metal but can be removed by heat treatment[22].

Interface stability of YSZ@BASE with Na metal. To investigate the interfacial stability, Na symmetric cells with YSZ@BASE or BASE membranes were fabricated and cycled at 80 °C. Swagelok-type cells with light springs (a stacking pressure of ~0.18 MPa) were employed for such tests (Fig. 2a and Supplementary Fig. 8). An optimum operating temperature of 80 °C was chosen to strike a balance between the battery performance and other considerations (safety, cost and durability) (Supplementary Figs. 9–11). The total EIS areal specific resistance (ASR) of the Na/YSZ@BASE/Na cells was 132.0 Ω cm^2 at RT (Fig. 2b and Supplementary Table 2). Once the contributions from the bulk and grain boundary were removed, the YSZ@BASE/Na interfacial ASR was found to be as low as 18.8 Ω cm^2 at RT. When the temperature was increased to 80 °C, the total EIS and interfacial ASRs further reduced to 23.1 and 3.6 Ω cm^2, respectively.

The voltage of the Na/YSZ@BASE/Na symmetric cell gradually decreased during the initial 20 cycles at 0.25 mA cm^{-2} (0.125 mAh cm^{-2} in capacity) and became stable at ~5 mV thereafter (Fig. 2c). It was further cycled at a fixed current of 0.5 mA cm^{-2} with a step-increased capacity from 0.5 to 2.5 mAh cm^{-2}. The voltage
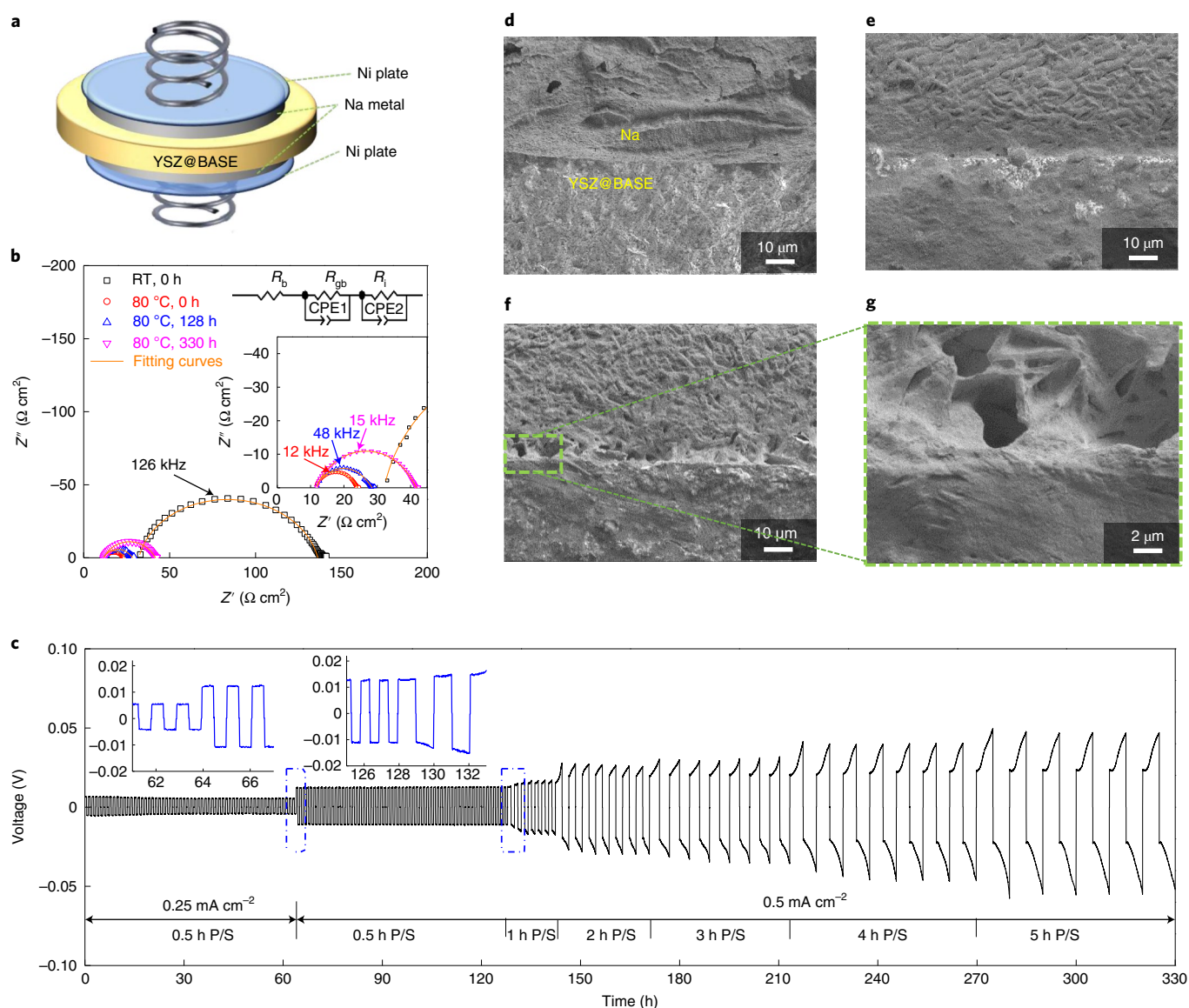
Fig. 2 | Characterization of the YSZ@BASE/Na interface at RT and 80 °C. a, Schematic configuration of a Na/YSZ@BASE/Na symmetric cell. **b**, Comparison of EIS profiles of the Na symmetric cells at RT and 80 °C with cycling times of 0 h, 128 h and 330 h. Top inset: the equivalent circuit model for fitting. R_b, bulk resistance; R_{gb}, grain boundary resistance; R_i, interfacial resistance; CPE1, constant phase element of grain boundary; CPE2, constant phase element of interface. Bottom inset: expansion of the lower left curves. **c**, Galvanostatic cycling of the Na symmetric cell at 80 °C and current densities of 0.25 and 0.50 mA cm^{-2} with varied Na plating/stripping (P/S) times. Insets: expansions to show the cycling within the dashed areas in detail. **d–f**, The corresponding SEM images of YSZ@BASE/Na interfaces at 80 °C with cycling times of 0 h (**d**), 128 h (**e**) and 330 h (**f**). **g**, Magnification of the dashed area in **f**.

curve becomes steeper as the capacity increases (Fig. 2c), which indicates a higher volume of pores and therefore Na depletion at the interface due to limited Na diffusion kinetics[24,25]. Overall, highly reversible Na plating/stripping with a small cell voltage (<50 mV) was achieved for YSZ@BASE cells even under a high areal capacity of 2.5 mAh cm^{-2}. In comparison, a Na/BASE/Na symmetric cell (Supplementary Fig. 12) exhibited a relative stable voltage of ~18 mV at 0.5 mA cm^{-2} and a low capacity of 0.25 mAh cm^{-2} during the initial 45 hours of cycling, but shorted at ~81 hours. The stable cycling of Na/YSZ@BASE/Na symmetric cells over 330 hours demonstrates that the YSZ@BASE/Na interface is more robust than that of BASE/Na under similar conditions. Note that the operating temperature (80 °C) is close to the Na melting point (97 °C), which is critical for maintaining the contact between the YSZ@BASE and the Na metal, and thus the extremely small interfacial resistance (Supplementary Fig. 13).

Interface structure and morphology of YSZ@BASE with Na metal. The intimate contact between the YSZ@BASE and the Na metal was observed before cycling at 80 °C (Fig. 2d). After a cycling time of 128 hours at a capacity of 0.25 mAh cm^{-2} (Fig. 2e), the intimate contact was still maintained. After the cell was cycled at a high capacity of 2.5 mAh cm^{-2}, quite a few large pores (~3 μm) were observed in the Na metal close to the interface (Fig. 2f,g). The pore formation is probably due to the volume expansion and shrinking during the Na plating and stripping, respectively.

The solid–electrolyte interphase (SEI) layer after cycling for 330 hours was analysed using ex situ scanning transmission electron microscopy (STEM). As indicated in Fig. 3a,b, an amorphous layer with a thickness of ~10 nm was observed between the YSZ@BASE bulk region (crystalline phase) and Na metal. The crystal structure of the bulk region was well maintained after the long-term cycling: Na-ion conduction planes and Al–O spinel
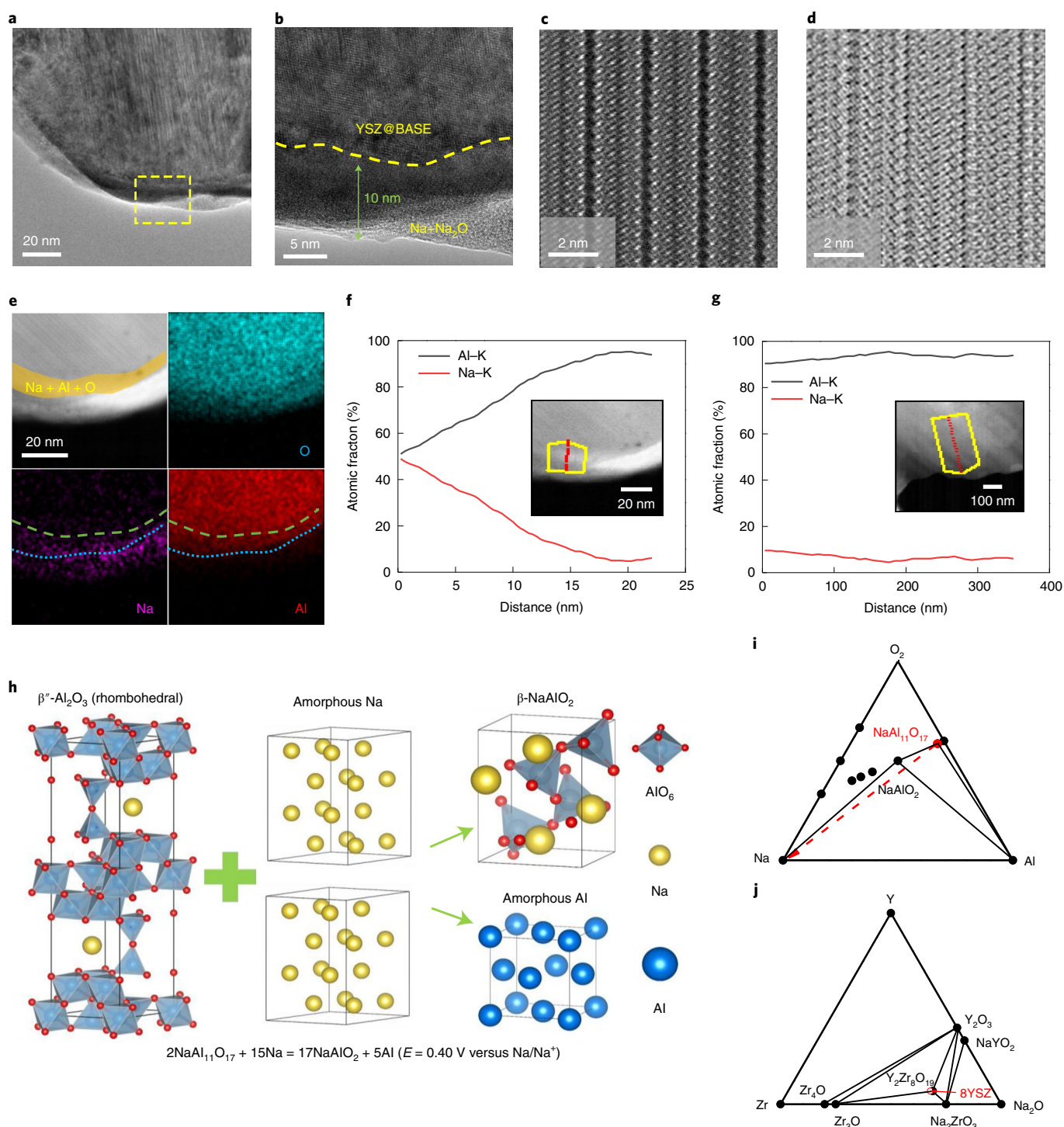
Fig. 3 | Fundamentals of YSZ@BASE/Na metal interfacial reaction at 80 °C. a, Typical TEM cross-section image of the global view at the YSZ@BASE/Na interface. **b**, High-resolution TEM image of a magnified view at the YSZ@BASE/Na interface. The yellow dashed line outlines the boundary between the crystalline and amorphous phases, in which the bulk region maintains a crystalline state and the interfacial parts are amorphous. **c,d**, HAADF-STEM (**c**) and annular bright-field-STEM (**d**) images of the YSZ@BASE bulk region. **e**, HAADF-STEM image of YSZ@BASE/Na interface and the corresponding EDS mappings of Na, Al and O atoms. The yellow marked area highlights the amorphous phase enriched with Na, Al and O atoms due to interfacial reactions. The green and blue dashed lines represent the upper and lower boundaries of the Na- and Al-enriched regions, respectively. **f,g**, TEM–EELS results of cycled YSZ@BASE showing the Al–K and Na–K profiles along the BASE/Na interface (**f**) and the bulk of BASE phase (**g**). Insets: the line-scan area and direction for the composition signals. **h**, Interface model of first-principles simulations for the BASE and Na, which demonstrates the formation of an interphase that contains Al and β-NaAlO₂ at 80 °C. **i**, Ternary phase diagram of the Na–Al–O₂ system, obtained from the MP. **j**, Corresponding Na–Y–Zr–O system in equilibrium with the Na metal from MP.
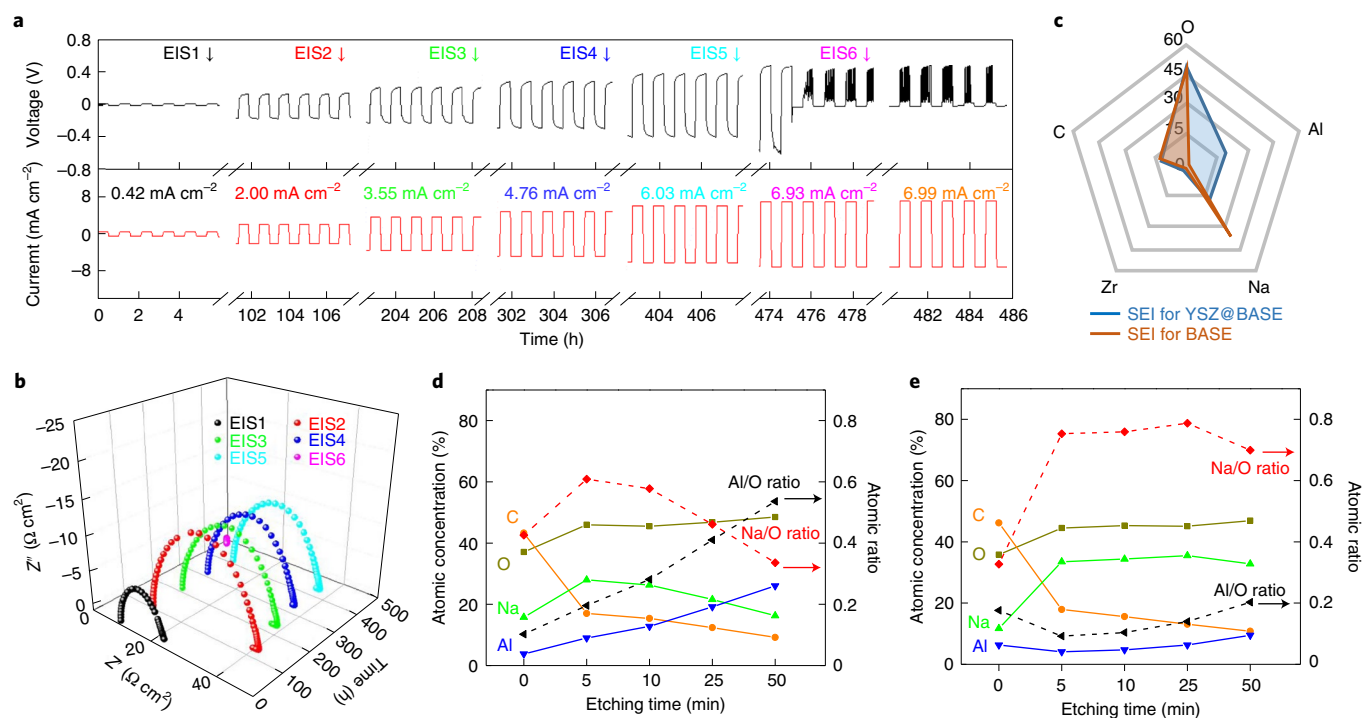
Fig. 4 | Dendrite suppression capability and interface chemistry of YSZ@BASE at 80 °C. a, Galvanostatic Na plating/stripping profiles in the symmetric cell at step-increased current densities (0.07 mA cm^{-2} per step) with a constant 30 min for plating/stripping. **b**, Corresponding EIS profiles during Na plating/ stripping cycles as marked in **a**. **c**, Comparison of the elemental concentration of the SEI formed on the cycled YSZ@BASE and BASE pellets after etching for 5 min. The SEI of YSZ@BASE that contained high concentrations of O and Al was β-NaAlO$_2$-rich, compared with the SEI on BASE that consisted of a large amount of Na$_2$O due to the continual reduction by Na. **d,e**, XPS elemental composition changes of cycled YSZ@BASE (**d**) and BASE pellets (**e**) after various durations of Ar$^+$ etching.

blocks were observed in high-angle annular dark-field STEM (HAADF-STEM) (Fig. 3c) and annular bright-field STEM (Fig. 3d) images. The HAADF-STEM image of the YSZ@BASE/ Na interface and the corresponding EDS mappings indicate that the SEI layer (green and blue dashed lines in Fig. 3e) is rich in Na, Al and O elements. The Na/Al atomic ratio based on line-scan electron energy loss spectroscopy (EELS) quantitative analysis decreases gradually from 50:50 (interface) to 10:90 (a depth of 15 nm in the BASE phase) (Fig. 3f). At the depth of 15 nm, the Na/ Al ratio is close to that in the bulk region (Fig. 3g). The change of Na/Al ratio along the BASE/Na interface for the cycled YSZ@ BASE confirms the formation of SEI composed of Na-Al-O compounds, which is consistent with our EDS mapping results in Fig. 3e. In addition, the Zr/Y ratio near the YSZ/Na interface varies with the location due to the reduction of YSZ and formation of a passivation layer (Supplementary Fig. 14).

These observations also agree with the first-principles calculations of chemical reactions between Na metal and β″-Al$_2$O$_3$ in YSZ@BASE (Fig. 3h). Based on the calculation, β″-Al$_2$O$_3$ is not thermodynamically stable with Na metal at 80 °C, which leads to the formation of β-NaAlO$_2$ and a small amount of Al metal with an equilibrium voltage of 0.4 V (versus Na/Na$^+$). Figure 3i shows a corresponding ternary phase diagram of Na–Al–O$_2$ obtained from the Materials Project (MP)[26]. The reactions between the β″-Al$_2$O$_3$ in YSZ@BASE and the Na metal led to the formation of a stable β-NaAlO$_2$ phase (~1 mS cm^{-1}) (ref. [27]), which prevented continuous reactions or corrosion in the subsequent cycling. The phase diagram of the Na–Y–Zr–O system in Fig. 3j also indicates that YSZ (red dot) becomes highly stable with Na metal by forming a passivating layer with a non-Na-conducting Y$_2$Zr$_8$O$_{19}$ interphase. The formation of such a chemically inert interphase along with a stable β-NaAlO$_2$-

containing SEI ensures a strong contact with the Na metal even at high currents and capacities during Na plating/stripping.

Dendrite suppression and interface chemistry of YSZ@BASE. Symmetric Na/YSZ@BASE/Na cells were cycled at step-increased current densities (0.07 mA cm^{-2} per step) for a fixed 0.5 hours to explore the Na dendrite suppression capability at 80 °C (Fig. 4a and Supplementary Figs. 15 and 16). At higher current densities (>2.00 mA cm^{-2}), the cell voltage presented a slope in both plating and stripping processes. Once the current density reached a critical value of 6.93 mA cm^{-2}, the cell experienced a sudden voltage drop (Fig. 4a), which indicates Na dendrite penetration across the electrolyte and a short circuit. Cell impedance spectra at several selected current densities were collected and are shown in Fig. 4b. The total ASRs of the cell are 24.0, 42.8, 40.3, 38.0 and 38.3 Ω cm^2 at 0.42, 2.00, 3.55, 4.75 and 6.03 mA cm^{-2}, respectively. In comparison, a Na symmetric cell with a pure BASE membrane exhibited an abrupt voltage drop and a short circuit at 1.5 mA cm^{-2} (Supplementary Fig. 17a). Fitted EIS profiles after cycling for 5 and 117 hours indicated that the cell had an overall ASR of 39.1 Ω cm^2, but this dropped to zero after the short circuit (Supplementary Fig. 17b,c). Overall, the CCD of thin YSZ@BASEs (0.47 mm) at a low pressure of 0.18 MPa reached a very high value of ~7.0 mA cm^{-2} at ~3.5 mAh cm^{-2}: one of the best performances so far among all the reported metal/SSE/metal systems at temperatures below 100 °C and with a mild stacking pressure (Supplementary Table 1.) Although the addition of YSZ to BASE increases the surface resistance and might lead to current constriction[28], our result shows it helps to increase the CCD and suppress dendritic growth. A similar result was reported by Aetukuri et al.[29]

YSZ@BASE and BASE membranes from the Na symmetric cells were further analysed using XPS. The SEI formed on the cycled
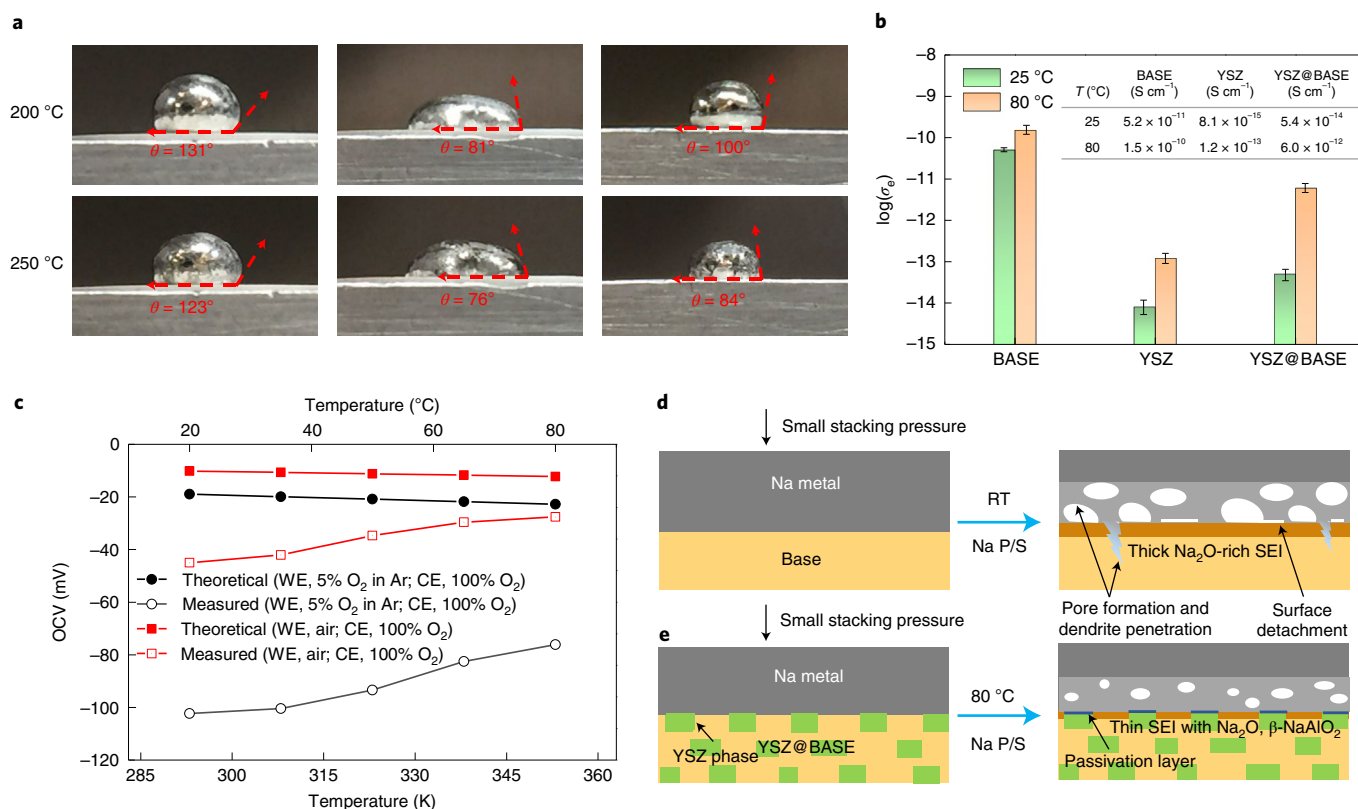
Fig. 5 | Stability mechanism of YSZ@BASE/Na interface at 80 °C. a, Wetting behaviours of molten Na on BASE (left), YSZ (middle) and YSZ@BASE (right) surfaces at elevated temperatures of 200 °C and 250 °C. **b**, Comparison of the electronic conductivities of BASE, YSZ@BASE and YSZ pellets at RT and 80 °C. σ_e, measure electronic conductivity. **c**, SEP measurement of a YSZ@BASE electrochemical cell showing the OCV between the working and counter electrodes as a function of temperature under different feed-gas conditions. The calculated values from the Nernst equation are also plotted for comparison. **d,e**, Schematics of the Na plating/stripping mechanisms for BASE (**d**) and YSZ@BASE (**e**) to illustrate the interface anchoring effect and interphase formation. CE, counter electrode; WE, working electrode.

YSZ@BASE is O and Al rich due to (1) the existence of β-NaAlO$_2$ (Figs. 3e and 4c) and (2) YSZ limiting the continual reduction of BASE (Supplementary Fig. 18). Compared with that of the BASE, the YSZ@BASE SEI layer contains less Na but more Al along the depth profile. The rapid increase in the Al/O ratio (from 0.10 to 0.54) and reduction in the Na/O ratio (from 0.61 to 0.34) along the profile indicates that the NaAlO$_2$-rich SEI formed on the YSZ@BASE is relatively thin due to the enhanced stability via the addition of YSZ (Fig. 4d). However, the nearly unchanged Na/O (0.70–0.75) and Al/O (0.09-0.2) ratios indicate that the BASE sample was covered with a much thicker Na$_2$O-rich SEI due to a continual reduction of β″-Al$_2$O$_3$ by sodium (Fig. 4e). The different surface chemistries for the cycled YSZ@BASE and BASE demonstrates the improvement of the Na surface stability of BASE via the addition of the YSZ phase.

Interface stability mechanism of YSZ@BASE. The excellent interface stability to Na and extremely high CCD of YSZ@BASE at 80 °C is primarily due to the existence of a 37% YSZ phase: (1) the addition of YSZ can significantly strengthen BASE; (2) YSZ is non-conductive and sodiophilic, which can maintain intimate contacts with Na metal during the plating and stripping, and (3) YSZ suppresses the colouration of β″-Al$_2$O$_3$, which led to the formation of a thin and robust β-NaAlO$_2$ SEI layer between Na and the β″-Al$_2$O$_3$ phase in the YSZ@BASE.

First, the addition of YSZ to BASE significantly enhances the overall mechanical strength. The shear and Young's moduli were as high as 102 and 253 GPa, respectively, superior to those of other SSEs for Li and Na batteries, which include both oxides, sulfide-based ionic conductors and pure BASE (Supplementary Table 3).

The calculated fracture toughness, which describes the capability of a material to resist crack propagation, is 1.8 MPa m^{-2} for YSZ@BASE (versus ~1 MPa m^{-2} for others). The enhanced fracture toughness can lead to an obvious improvement in its CCD due to suppression of the dendrite penetration[30–33].

Second, the YSZ phase in YSZ@BASE can enhance the Na wetting (or bonding). Figure 5a shows the wettability of molten Na on the BASE, YSZ and YSZ@BASE substrates at 200 and 250 °C. At both temperatures, the Na wetting was better on the YSZ@BASE substrate than that on BASE (for example, 100 versus 131° at 200 °C) and the best performance was achieved on the YSZ substrate (81°). Besides, the surface adhesion energy W for the YSZ/Na interface ($W_{YSZ/Na}$), based on a molecular dynamics (MD) simulation, is −0.29 eV Å^{-2}, which is much larger than that for the BASE/Na interface (−0.22 eV Å^{-2}) (Supplementary Fig. 19). All of these results demonstrated the improved sodiophilic property and bonding with the addition of the YSZ phase to the BASE.

Third, the Na dendrite can deposit in BASE (colouration of BASE). The electronic conduction of BASE increased due to the reduction of β″-Al$_2$O$_3$ by Na. The reduction of β″-Al$_2$O$_3$ formed oxygen vacancies near the interface, which resulted in a continual electron compensation for the oxygen vacancy, which enhanced electronic conductivity of BASE and caused Na dendrite deposition inside of the electrolyte[19,34]. The reaction is given as:

$$2\mathrm{Na_E} + (\mathrm{O_o})_\beta \rightarrow (\mathrm{Na_2O}) + (\mathrm{V_{\ddot{o}}})_\beta + 2\left(e'\right)_\beta$$
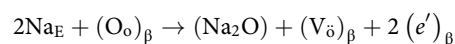
The subscript β refers to BASE and the subscript E to the sodium electrode. Here, the YSZ phase has dual functions: (1) It decreases
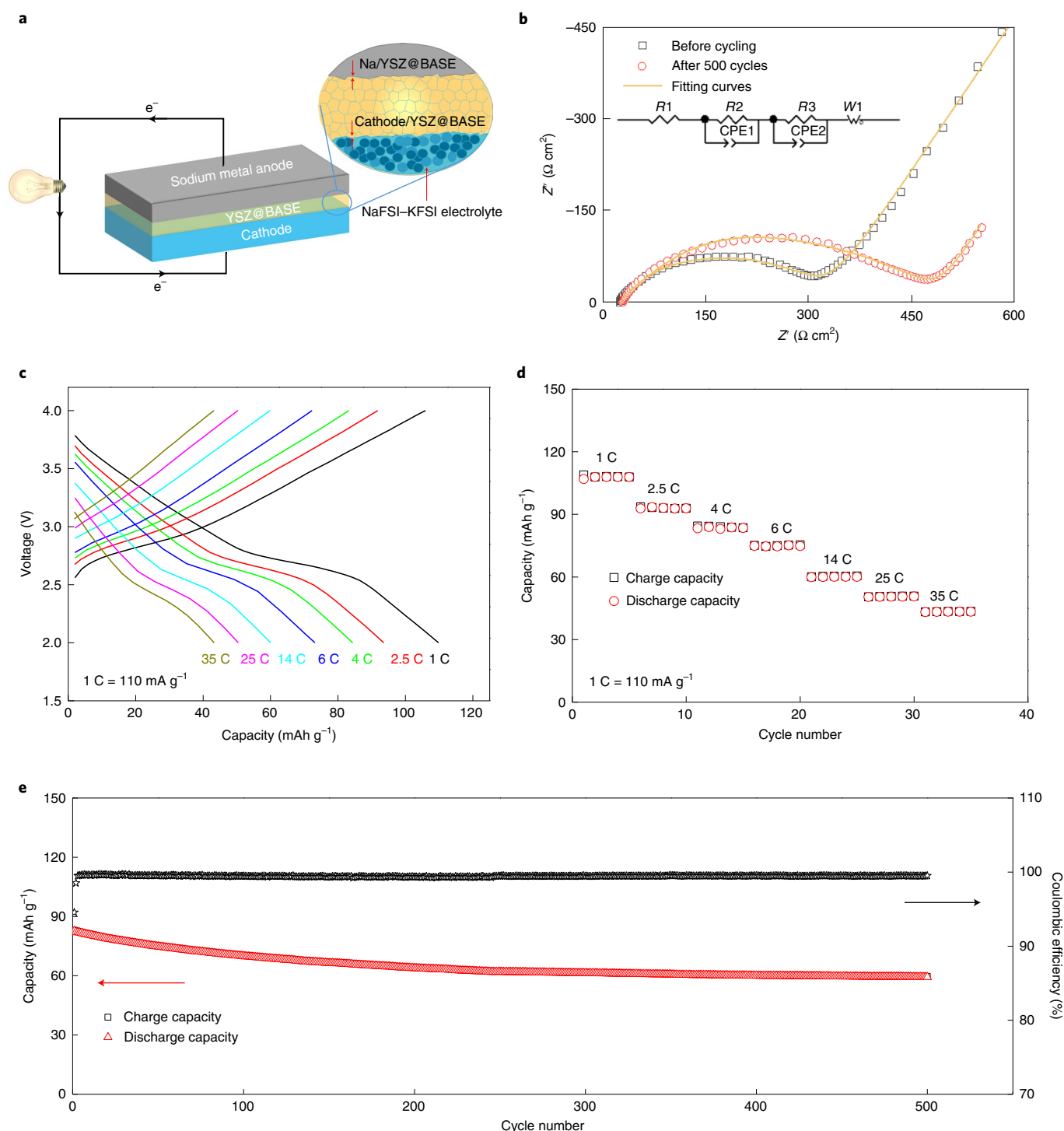
Fig. 6 | Demonstration of a high-voltage cell with a YSZ@BASE and Na anode. a, Schematic of the designed quasi-solid cell using a Na anode, YSZ@BASE electrolyte, NaFSI–KFSI electrolyte and NaNCMT/carbon-black/poly(vinyl difluoride) composite cathode. Inset: enlarged view of the interfaces between the YSZ@BASE and the electrodes after interfacial engineering. **b**, Nyquist spectra and fitting results of the solid cell before and after 500 cycles at 80 °C. Inset: the equivalent circuit model for fitting. *R*1, electrolyte resistance; *R*2/*R*3, anode/cathode interfacial resistance; CPE1/CPE2, constant phase element of anode/cathode interface; *W*1 Warburg diffusion element. **c**, Rate performance of the cell at C rates of 1–35C at 80 °C. **d**, The corresponding galvanostatic charge/discharge curves at different C rates. **e**, Cycling performance of the cell at 4C. 1C = 110 mA g⁻¹, and the loading of active material is 2–3 mg cm⁻².

the overall electronic conductivity of YSZ@BASE. The measured electronic conductivities σ_e of BASE and YSZ are 5.2×10^{-11} and 8.1×10^{-15} S cm⁻¹ at RT, respectively (Fig. 5b and Supplementary Fig. 20)[22,35]. The addition of 37 wt% YSZ to BASE achieved an electronic conductivity of 5.4×10^{-14} S cm⁻¹ at RT, which is significantly lower than those of pure BASE and other SSEs, such as $Li_7La_3Zr_2O_{12}$ and Li_3PS_4 (10^{-9}–10^{-8} S cm⁻¹ at RT)[36–38]. YSZ@BASE shows a slightly higher electronic conductivity at 80 °C (6.0×10^{-12} S cm⁻¹) but is still around two orders of magnitude lower than that of pure BASE, which is believed to be helpful for suppressing Na dendrite

formation[37]. (2) O^{2+}-conducting YSZ can also suppress the colouration of BASE. The oxygen conduction of YSZ@BASE at low temperatures was confirmed using solid electrolyte potentiometry (SEP), which was originally proposed by Wagner[39] (Fig. 5c and Supplementary Fig. 21). The observed open circuit voltage (OCV) and electrochemical electrode reactions confirmed oxygen-ion conduction in the YSZ phase of YSZ@BASE at 80 °C. Molten Na can cause BASE surface degradation (so-called colouration), in which the produced oxygen vacancies are chargely compensated by electrons[40–42]. The continual reduction of BASE forms a thick Na_2O-rich SEI with a high electronic conductivity and finally shorts the cell by deposited Na and residual Al. However, in the YSZ@BASE, the well-mixed YSZ phase with a high oxygen fugacity tends to supply oxygen ions for the surface oxygen vacancies in the BASE and thus suppress its colouration, which leads to the formation of a thin and β-$NaAlO_2$-rich SEI. The high oxygen fugacity of the YSZ is due to the high-temperature sintering under an O_2-rich atmosphere. In addition, the reduction of Na reactivity and bulk electronic conductivity by lowering the operating temperature can also relieve the process of BASE colouration, and thus improve the cycle stability of the cell with YSZ@BASE.

In summary, thick Na_2O-rich SEI and large pores can be formed near the BASE/Na interface at RT. Surface detachment may also occur under a small stacking pressure and large current and/or capacity cycling conditions, and result in the formation of localized hot spots for dendrite-like Na nucleation (Fig. 5d and Supplementary Fig. 22)[43,44]. Through the introduction of the Na^+ insulating and O^{2-} conducting YSZ phase, a thin and dense SEI that consists of β-$NaAlO_2$ and Na_2O can be formed, which helps stabilize the YSZ@BASE/Na interface. It was also found that YSZ has better sodiophilic properties than BASE. Given that the Na metal does not experience a plating and stripping process on the YSZ surface, we propose a new concept of an 'interface anchoring effect' for the YSZ@BASE/Na interface (Fig. 5e). The anchoring effect between the Na and YSZ surface helps avoid the surface detachment during the plating and stripping, and thus enables a strong contact at the interface even under extremely high current densities.

Full-cell performance with Ni-rich cathodes. By coupling with a high-voltage layered O_3–$NaNi_{0.45}Cu_{0.05}Mn_{0.4}Ti_{0.1}O_2$ (NaNCMT) cathode[45], a quasi-solid-state Na/YSZ@BASE/NaNCMT full cell was fabricated (Fig. 6a). To reduce the interfacial resistance between the YSZ@BASE and the cathode, an eutectic salt that consisted of sodium bis(fluorosulfonyl)imide and potassium bis(fluorosulfonyl)imide (NaFSI–KFSI, molar ratio of 44:56) was applied as the wetting agent between the YSZ@BASE electrolyte and the NaNCMT cathode. At 80 °C, the NaFSI–KFSI eutectic salt was in a liquid state with a high Na-ion conductivity (1.3 mS cm^{-1}) and excellent oxidation stability (>4.5 V), and thus can be used as the wetting agent to reduce the interfacial resistance (Supplementary Figs. 23–25)[46,47].

The Na/YSZ@BASE/NaNCMT cells exhibited a low initial cell resistance (300 Ω cm^2) (Fig. 6b) and a high rate capability (Fig. 6c,d) at 80 °C. The cell capacity was ~110 mAh g^{-1} at a 1C rate (1C = 110 mA g^{-1}), which is close to the theoretical value of the NaNCMT cathode (that is, ~124 mAh g^{-1}). The battery delivers high capacities of 84, 60 and 43 mAh g^{-1} at rates of 4C, 14C and 35C, respectively, which confirms the excellent rate capability of the battery. Note that the operation of the full cell at a current density higher than the CCD is possible given that the areal capacity (0.25 mAh cm^{-2} at 35 C) is much less than the areal capacity (3.5 mAh cm^{-2}) for the CCD measurement. CCD generally increases with a decrease in the areal capacity, so its value measured at 0.25 mAh cm^{-2} should be higher than the current one (~7 mA cm^{-2}). The cell also shows good long-term stability at a rate of 4C (1.0 mA cm^{-2}), with a capacity retention of 73% over 500 cycles and a high coulombic efficiency of >99.99% (Fig. 6e). After 500 cycles, the ASRs of the electrolyte were almost unchanged, whereas the interfacial resistances (R2 + R3) for the Na/YSZ@BASE/NaNCMT cell increased from 279.0 to 465.8 Ω cm^2 (Fig. 6b and Supplementary Table 4). The excellent performance of the full cell is attributed to the formation of a stable passivation layer or cathode–electrolyte interphase (CEI) (Supplementary Fig. 26), which prevents a continual surface and/or structural degradation of the cathode. The CEI formation mechanism was demonstrated by HAADF-STEM (Supplementary Figs. 27 and 28), ab initio MD calculation (Supplementary Fig. 29) and XPS analysis (Supplementary Fig. 30).

Conclusions

By introducing YSZ into β″-Al_2O_3 electrolyte and adding eutectic NaFSI-KFSI molten salt between the YSZ@BASE and the NaNCMT cathode, we significantly reduced the interfacial resistance, which ensured Na/YSZ@BASE/NaNCMT full cells maintained a low overall resistance (300–500 Ω cm^2), high rate performance and good cycling stability during 500 cycles. In a typical Na/YSZ@BASE/Na symmetric cell, the initial interfacial resistance was as low as 3.6 Ω cm^2 and stable for over 300 hours. CCD of the YSZ@BASE electrolyte reached ~7.0 mA cm^{-2} at a capacity of ~3.5 mAh cm^{-2}, which is almost five times higher than that of pure BASE (~1.5 mA cm^{-2}) under similar testing conditions and is very high among all the SSE/metal systems. YSZ plays a critical role in suppressing the Na dendrite penetration by enhancing the fracture toughness and lowering the overall electronic conduction of YSZ@BASE, which can prevent internal Na deposition. As an oxygen-ion conductor, YSZ can also transport oxygen ions and thus eliminate oxygen vacancies caused by BASE reduction, which leads to formation of a thin and stable β-$NaAlO_2$-rich SEI, rather than a thicker Na_2O-rich SEI for BASE.

Online content

Any methods, additional references, Nature Research reporting summaries, source data, extended data, supplementary information, acknowledgements, peer review information; details of author contributions and competing interests; and statements of data and code availability are available at https://doi.org/10.1038/s41565-021-01036-6.

References

1. Tarascon, J. M. Is lithium the new gold? *Nat. Chem.* **2**, 510 (2010).
2. Slater, M. D., Kim, D., Lee, E. & Johnson, C. S. Sodium-ion batteries. *Adv. Funct. Mater.* **23**, 947–958 (2013).
3. Fan, X. et al. High-performance all-solid-state Na–S battery enabled by casting–annealing technology. *ACS Nano* **12**, 3360–3368 (2018).
4. Zhou, W., Li, Y., Xin, S. & Goodenough, J. B. Rechargeable sodium all-solid-state battery. *ACS Cent. Sci.* **3**, 52–57 (2017).
5. Zhao, C. et al. Solid-state sodium batteries. *Adv. Energy Mater.* **8**, 1703012 (2018).
6. Goodenough, J. B., Hong, H.-P. & Kafalas, J. Fast Na^+-ion transport in skeleton structures. *Mater. Res. Bull.* **11**, 203–220 (1976).
7. Lu, Y., Li, L., Zhang, Q., Niu, Z. & Chen, J. Electrolyte and interface engineering for solid-state sodium batteries. *Joule* **2**, 1747–1770 (2018).
8. Hou, W. et al. Solid electrolytes and interfaces in all-solid-state sodium batteries: progress and perspective. *Nano Energy* **52**, 279–291 (2018).
9. Hayashi, A., Noi, K., Sakuda, A. & Tatsumisago, M. Superionic glass-ceramic electrolytes for room-temperature rechargeable sodium batteries. *Nat. Commun.* **3**, 856 (2012).
10. Berbano, S. S., Seo, I., Bischoff, C. M., Schuller, K. E. & Martin, S. W. Formation and structure of $Na_2S + P_2S_5$ amorphous materials prepared by melt-quenching and mechanical milling. *J. Non Cryst. Solids* **358**, 93–98 (2012).
11. Heo, J. W., Banerjee, A., Park, K. H., Jung, Y. S. & Hong, S.-T. New Na-ion solid electrolytes $Na_{4-x}Sn_{1-x}Sb_xS_4$ (0.02 ≤ x ≤ 0.33) for all-solid-state Na-ion batteries. *Adv. Energy Mater.* **8**, 1702716 (2018).
12. Lu, X., Xia, G., Lemmon, J. P. & Yang, Z. Advanced materials for sodium–beta alumina batteries: status, challenges and perspectives. *J. Power Sources* **195**, 2431–2442 (2010).

13. Lu, X. et al. Liquid–metal electrode to enable ultra-low temperature sodium–beta alumina batteries for renewable energy storage. *Nat. Commun.* **5**, 4578 (2014).
14. Näfe, H., Fritz, M. & Lorenz, W. On the defect electron conduction parameter of Na·beta-alumina. *Solid State Ion* **74**, 275–278 (1994).
15. Lu, X. et al. Advanced intermediate-temperature Na–S battery. *Energy Environ. Sci.* **6**, 299–306 (2013).
16. Li, G. et al. Advanced intermediate temperature sodium–nickel chloride batteries with ultra-high energy density. *Nat. Commun.* **7**, 10683 (2016).
17. Wen, Z. et al. Research on sodium sulfur battery for energy storage. *Solid State Ion* **179**, 1697–1701 (2008).
18. Wen, Z. et al. Research activities in Shanghai Institute of Ceramics, Chinese Academy of Sciences on the solid electrolytes for sodium sulfur batteries. *J. Power Sources* **184**, 641–645 (2008).
19. De Jonghe, L. C., Feldman, L. & Beuchele, A. Slow degradation and electron conduction in sodium/beta-aluminas. *J. Mater. Sci.* **16**, 780–786 (1981).
20. Williams, R. M. et al. The thermal stability of sodium beta"-alumina solid electrolyte ceramic in AMTEC cells. In *Space Technology and Applications International Forum* 1306–1311 (AIP, 1999).
21. Ansell, R. The chemical and electrochemical stability of beta-alumina. *J. Mater. Sci.* **21**, 365–379 (1986).
22. Bay, M. C. et al. Sodium plating from Na-β″-alumina ceramics at room temperature, paving the way for fast-charging all-solid-state batteries. *Adv. Energy Mater.* **10**, 1902899 (2020).
23. Lacivita, V., Wang, Y., Bo, S.-H. & Ceder, G. Ab initio investigation of the stability of electrolyte/electrode interfaces in all-solid-state Na batteries. *J. Mater. Chem. A* **7**, 8144–8155 (2019).
24. Krauskopf, T., Mogwitz, B., Rosenbach, C., Zeier, W. G. & Janek, J. Diffusion limitation of lithium metal and Li–Mg alloy anodes on LLZO type solid electrolytes as a function of temperature and pressure. *Adv. Energy Mater.* **9**, 1902568 (2019).
25. Kasemchainan, J. et al. Critical stripping current leads to dendrite formation on plating in lithium anode solid electrolyte cells. *Nat. Mater.* **18**, 1105–1111 (2019).
26. Jain, A. et al. Commentary: The Materials Project: a materials genome approach to accelerating materials innovation. *APL Mater.* **1**, 011002 (2013).
27. Bianchini, F., Fjellvag, H. & Vajeeston, P. A first principle comparative study of the ionic diffusivity in $LiAlO_2$ and $NaAlO_2$ polymorphs for solid-state battery applications. *Phys. Chem. Chem. Phys.* **20**, 9824–9832 (2018).
28. Krauskopf, T., Richter, F. H., Zeier, W. G. & Janek, J. R. Physicochemical concepts of the lithium metal anode in solid-state batteries. *Chem. Rev.* **120**, 7745–7794 (2020).
29. Aetukuri, N. B. et al. Flexible ion-conducting composite membranes for lithium batteries. *Adv. Energy Mater.* **5**, 1500265 (2015).
30. Cho, Y.-H. et al. Mechanical properties of the solid Li-ion conducting electrolyte: $Li_{0.33}La_{0.57}TiO_3$. *J. Mater. Sci.* **47**, 5970–5977 (2012).
31. Krauskopf, T., Hartmann, H., Zeier, W. G. & Janek, J. Toward a fundamental understanding of the lithium metal anode in solid-state batteries-an electrochemo-mechanical study on the garnet-type solid electrolyte $Li_{6.25}Al_{0.25}La_3Zr_2O_{12}$. *ACS Appl. Mater. Interfaces* **11**, 14463–14477 (2019).
32. Kim, Y. et al. The effect of relative density on the mechanical properties of hot-pressed cubic $Li_7La_3Zr_2O_{12}$. *J. Am. Ceram. Soc.* **99**, 1367–1374 (2016).
33. Wolfenstine, J., Allen, J. L., Sakamoto, J., Siegel, D. J. & Choe, H. Mechanical behavior of Li-ion-conducting crystalline oxide-based solid electrolytes: a brief review. *Ionics* **24**, 1271–1276 (2017).
34. De Jonghe, L. C. Transport number gradients and solid electrolyte degradation. *J. Electrochem. Soc.* **129**, 752–755 (1982).
35. Zhang, L., Zhu, L. & Virkar, A. V. Electronic conductivity measurement of yttria-stabilized zirconia solid electrolytes by a transient technique. *J. Power Sources* **302**, 98–106 (2016).
36. Rangasamy, E., Wolfenstine, J. & Sakamoto, J. The role of Al and Li concentration on the formation of cubic garnet solid electrolyte of nominal composition $Li_7La_3Zr_2O_{12}$. *Solid State Ion* **206**, 28–32 (2012).
37. Han, F. et al. High electronic conductivity as the origin of lithium dendrite formation within solid electrolytes. *Nat. Energy* **4**, 187–196 (2019).
38. Shin, B. R. et al. Comparative study of TiS_2/Li–In all-solid-state lithium batteries using glass-ceramic Li_3PS_4 and $Li_{10}GeP_2S_{12}$ solid electrolytes. *Electrochim. Acta* **146**, 395–402 (2014).
39. Wagner, C. Adsorbed atomic species as intermediates in heterogeneous catalysis. *Adv. Catal.* **21**, 323–381 (1970).
40. De Jonghe, L. C. & Buechele, A. Chemical colouration of sodium beta-aluminas. *J. Mater. Sci.* **17**, 885–892 (1982).
41. De Jonghe, L. C., Buechele, A. & Armand, M. Oxygen interstitial transport and chemical coloration in sodium-beta alumina. *Solid State Ion.* **9**, 165–168 (1983).
42. Weber, N. A thermoelectric device based on beta-alumina solid electrolyte. *Energy Convers.* **14**, 1–8 (1974).
43. Westover, A. S., Dudney, N. J., Sacci, R. L. & Kalnaus, S. Deposition and confinement of Li metal along an artificial Lipon–Lipon interface. *ACS Energy Lett.* **4**, 651–655 (2019).
44. Porz, L. et al. Mechanism of lithium metal penetration through inorganic solid electrolytes. *Adv. Energy Mater.* **7**, 1701003 (2017).
45. Yao, H. R. et al. Designing air-stable O_3-type cathode materials by combined structure modulation for Na-ion batteries. *J. Am. Chem. Soc.* **139**, 8440–8443 (2017).
46. Fukunaga, A. et al. Intermediate-temperature ionic liquid NaFSA–KFSA and its application to sodium secondary batteries. *J. Power Sources* **209**, 52–56 (2012).
47. Kubota, K., Nohira, T., Goto, T. & Hagiwara, R. Novel inorganic ionic liquids possessing low melting temperatures and wide electrochemical windows: binary mixtures of alkali bis(fluorosulfonyl)amides. *Electrochem. Commun.* **10**, 1886–1888 (2008).

Methods

Materials. The YSZ@BASE discs were prepared using a vapour phase process, as described previously[12,13]. α-Al$_2$O$_3$ (Almatis, >99.8%), YSZ (8YSZ, UCM Advanced Ceramics), dispersant (Phospholan PS-236, Akzo Nobel), solvent (methyl ethyl ketone/ethanol), plasticizer (benzyl butyl phthalate, Aldrich), and binder (Butvar B-79) were thoroughly mixed to make a slurry. The slurry was cast into thin sheets, and then laminated and laser-cut into circular discs. The prepared discs were then sintered at 1,600 °C in air to achieve a high relative density of >99%. The sintered α-Al$_2$O$_3$/YSZ discs were then covered with loose β″-Al$_2$O$_3$ powder and heat treated at 1,450 °C in air to convert the α-Al$_2$O$_3$ into β″-Al$_2$O$_3$. The β″-Al$_2$O$_3$ powder used for the conversion process was synthesized separately via a solid-state reaction. The thickness of the converted YSZ@BASE discs was ~470 μm. The density was measured by the Archimedes method using ethanol as the immersion medium. For comparison, pure BASE pellets (diameter 10 mm, thickness 500 μm) without YSZ (relative density >98%) were bought from Ionotec. YSZ pellets (8YSZ, diameter 20 mm, thickness 250–300 μm) with high relative density of ~99% were purchased from Fuelcell Materials.

Cu- and Ti-co-doped O3-type NaNCMT was synthesized via a simple solid-state method reported previously[45]. Stoichiometric amounts of Na$_2$CO$_3$ (Alfa Aesar, 99.5%), NiO (Alfa Aesar, 99%), CuO (Alfa Aesar, 99%), Mn$_2$O$_3$ (Alfa Aesar, 98%) and TiO$_2$ (Alfa Aesar, 99.9%) were thoroughly mixed using ball milling and then pressed into pellets. To compensate for sodium loss during high-temperature sintering, an excess 5 mol% of Na$_2$CO$_3$ was added to the precursors. The precursor pellet was subsequently calcinated at 1,000 °C in air for 10 h to obtain the O3-type active material. A NaNCMT cathode was prepared by mixing as-synthesized NaNCMT, Super P carbon and poly(vinyl difluoride) binder (mass ratio of 8:1:1) with anhydrous N-methyl-2-pyrrolidone as a solvent to form a homogeneous slurry. The slurry was coated on Al foil and dried at 80 °C overnight in a vacuum to achieve a cathode film. The film was cut into discs with a diameter of 1.27 cm (0.5 inch) and stored in an Ar-filled glove box for further use. The loading mass of active material in the cathode was 2–3 mg cm^{-2}.

Material characterizations. Powder XRD data were collected between 6 and 100° (2θ) in 0.02° steps and 4 s per step using a Rigaku Miniflex II Bragg–Brentano diffractometer with Cu Kα radiation (λ = 1.5418 Å) and a graphite postdiffraction monochromator. Phases were identified and quantified by full-pattern (Rietveld) refinement using the program TOPAS (v. 4.2, Bruker AXS)[48]. Crystal structures for this analysis were obtained from the Inorganic Crystal Structure Database (Fachinformationszentrum Karlsruhe) and peak shapes were modelled using the fundamental parameters approach[49]. The patterns were collected without the addition of an internal standard and phase quantities were therefore scaled to 100%. Any amorphous or unidentified diffracting material was neglected. Cell dimensions and microstructural parameters were refined for phases with a concentration higher than 5 wt%.

XPS analysis was carried out using a Physical Electronics Quantera scanning X-ray microprobe, which was outfitted with a monochromatic Al Kα X-ray source (1,486.7 eV) for excitation. Cycled cathodes were rinsed with dimethyl carbonate in an Ar-filled glove box several times and dried under vacuum prior to characterization. Contents of different species in the catholyte–electrolyte interphase layer were obtained by fitting the entire XPS spectra using CasaXPS software. Thermogravimetric analysis of the Na/KFSI catholyte was conducted on a TGA-DSC instrument (Cahn TG2131) under an Ar atmosphere with a heating rate of 2 °C min^{-1}. Some of the SEM and high-resolution transmission electron microscopy characterizations in the present work were taken at the University of Maryland using a Hitachi SU-70 analytical GEG SEM and JEOL JEM 2100 LaB$_6$ transmission electron microscope with an electron accelerating voltage of 200 keV.

Focused ion beam (FIB)/SEM imaging and TEM specimen preparation were conducted at the Pacific Northwest National Laboratory on an FEI Helios Dual-Beam FIB operated at 2–30 kV. Thin-section TEM specimens of the Na–YSZ@BASE interface were prepared directly from cycled symmetric Na cells by a standard lift-out procedure. First, a 1.2-μm-thick Pt layer (200 nm electron-beam deposition followed by a 1 μm ion-beam deposition) was deposited on a region to avoid Ga ion-beam damage in the subsequent lift-out and thinning process. After the sample was lifted out, it was thinned to 200 nm using a 30 kV Ga ion beam. Then, a 2 kV final polishing was performed to remove surface damage, until there was electron transparency at 5 kV SEM imaging. After the 2 kV Ga ion polish, the surface damage layer was less than 1 nm. The FIB-prepared NaNCMT cathode samples were investigated using an FEI Titan 80-300 STEM microscope at 300 kV. The microscope was equipped with a probe spherical aberration corrector, which enabled sub-Ångström imaging using STEM-HAADF detectors. For STEM-HAADF imaging, the inner and outer collection angles of the annular dark-field detector were set at 55 and 220 mrad, respectively. STEM–EDS and STEM–electron energy loss spectroscopy were performed on a probe aberration-corrected JEOL JEM-ARM200CF S/TEM instrument at 200 kV.

The sessile drop technique was used to measure the contact angle of liquid sodium on BASE, YSZ and YSZ@BASE surfaces, as described previously[13,50]. High-purity Na (Alfa Aesar, 99.95%) was employed for the tests and the as-received clean BASE, YSZ and YSZ@BASE sample, without further surface modifications or treatments, were heated on a hot plate in an Ar-protected glove box to the desired

temperatures. Then, drops of liquid Na were transferred to the surface of the samples using a glass pipette. The wettability test was carried out at temperatures of 200 and 250 °C with a holding time of 30 min at each temperature for wetting-angle measurements.

Elastic properties of the BASE and YSZ@BASE, which included shear (G) and Young's (E) modulus, were measured using the pulse–echo method[51]. Ceramic discs with a thickness of 2.5 mm were carefully polished on both sides before determining the elastic properties. An ultrasonic source device (Sonic 137, Staveley) generated the ultrasonic pulse and an oscilloscope (Tektronix TDS220) recorded the echo signals. To determine fracture strength (σ$_f$), we applied the ball-on-ring test[52] using a universal testing machine (Model 4204, Instron). Fracture toughness (K$_{IC}$) was calculated based on the equation:

$$K_{IC} = \sigma_f \sqrt{\pi a_c}$$

The critical flaw size (a$_c$) for ceramics can be either the pore or the grain size. Here, we chose a pore or crack size of 4 μm based on the SEM image in Fig. 1c.

Electrochemical measurements. All the cell assembly/disassembly procedures were performed in an Ar-filled glove box with the moisture and O$_2$ contents below 2 ppm. The cell case utilized in this study was a Swagelog-type cell with light springs (Supplementary Fig. 8), which provides a stacking pressure of ~0.18 MPa during testing. The preparation of the SSE-composite electrode to investigate the oxidation stability of the SSE was reported previously[53]. To prepare carbon-coated YSZ@BASE particles, the as-prepared YSZ@BASE powders were ground using a high-energy vibrating mill (SPEX SamplePrep 8000M Mixer/Mill) for 1 h, dispersed into a solution of polyvinylpyrrlidone (10 wt% in ethanol) and then vigorously stirred for 30 min. The slurry was finally dried and sintered at 700 °C for 1 h in a flowing Ar atmosphere to enable carbon coating. The YSZ@BASE composite electrodes were prepared via hand mixing the carbon-coated YSZ@BASE particles and carbon black (40:60 by weight ratio) in the mortar. Then, 10 wt% poly(vinyl difluoride) and N-methyl-2-pyrrolidone were added to the mixture to make an electrode slurry. To make a Na/YSZ@BASE/YSZ@BASE-C cell, the YSZ@BASE electrode slurry was coated on the surface of a YSZ@BASE pellet, dried at 120 °C overnight and then sputtered with Au to improve the electrical contact. Na metal was subsequently attached to the other side of the pellet and cured at 80 °C to enhance the interfacial contact between the Na and the YSZ@BASE. The cyclic voltammogram of the Na/YSZ@BASE/YSZ@BASE-C cell was performed between 3.0 and 7.0 V with a scan rate of 0.05 mV s^{-1}. The CV measurements were carried out on an electrochemistry workstation (Solartron 1287/1260).

Na–SSE–Na symmetric cell assembly. Two identical fresh Na thin discs with a diameter of 1.27 cm (0.5 inch) were hand-pressed on both sides of a SSE (BASE or YSZ@BASE) pellet. Nickel plates with light springs were placed on top of the sodium discs (Fig. 2a) and the entire assembly was then placed into a Swagelok cell. The as-assembled Swagelok cells were tested on an Electrochemical Interface (Solartron 1287, Solartron Analytical) and a Frequency Response Analyzer (Solartron 1260, Solartron Analytical) for the EIS measurements at RT and at 80 °C. The frequency range was from 2 MHz to 0.01 Hz and the a.c. amplitude was 10 mV. The EIS data were analysed using ZView fitting software (Scribner Associates). The plating/stripping curves were collected with a battery-test system (BT2000, Arbin Instruments).

Na/YSZ@BASE/NaNCMT full cell. The NaFSI (Solvionic, 99.7%) and KFSI (Synthonix, 98%) salts were dried at 110 °C overnight under vacuum conditions before use. The NaFSI–KFSI mixture (molar ratio of 44:56) was heated to 130 °C to obtain a clear, molten solution (Supplementary Fig. 23a). A YSZ@BASE disc was heated to the same temperature on a hot plate. A tiny amount of the molten solution was subsequently applied on the BASE disc. Then, a piece of the NaNCMT cathode was soaked in the molten salt solution. After the electrolyte/catholyte/cathode assembly had cooled to RT, a piece of the sodium disc and a nickel plate, along with a spring, were attached to the opposite side of the BASE disc in sequence. The assembled Swagelok cells were then subjected to galvanostatic charge/discharge and EIS measurements at 80 °C. The current density was calculated based on the active materials of the cathode, where 1C (110 mA g^{-1}) corresponded to 0.2–0.3 mA cm^{-2} based on the area of the electrode.

Au/SSE/Au ion-blocking cells. A thin layer of Au (thickness ~300 nm, diameter 8 mm) was sputtered on each side of an SSE (BASE, YSZ or YSZ@BASE) pellet using a sputter coater (Cressington 108auto). The edge of the SSEs was covered with tape to prevent short circuit during the sputtering. The Au/SSE/Au cells were then assembled in Swagelok-type cells (Supplementary Fig. 8) and tested with a potentiostat (BioLogic) under different d.c. voltages and temperatures.

Solid electrolyte potentiometry measurement. The electrochemical concentration cell for the SEP measurements is shown in Supplementary Fig. 21a. An SSE disc (BASE, YSZ or YSZ@BASE) was glass sealed to an outer α-Al$_2$O$_3$ ring. Pt films with a thickness of ~500 nm and an active area of ~3 cm^2 were then symmetrically sputtered on both sides of the SSE disc as the WE and CE. The current collectors

for both the WE and CE were Ni foils. Two metal end plates were then compression sealed to both sides of the α-Al$_2$O$_3$ ring using rubber O rings. Conical springs were employed to connect the two current collectors with the two end plates. The feed gas for the WE chamber was either 5% O$_2$/95% Ar or air, and 100% O$_2$ was used for the CE chamber. The gas flow rate was 100 ml min^{-1}. The OCV of the cell was measure using a BioLogic battery cycler between 20 and 85 °C with an interval of 15 °C. The cell was set at each temperature for 1 h prior to the measurement.

Simulation method. All density functional theory calculations were performed using the Vienna ab initio simulation package[54] with the projector augmented wave approach[55]. The Perdew–Burke–Ernzerhof form of the generalized gradient approximation functionals was used to describe the exchange-correlation energy[56]. The ion–electron interaction was described with the projector augmented wave method. Spin-polarized total energy calculations and structure relaxations were performed. The voltage plateaus were obtained using the calculated density functional theory energies of all the relevant compounds in the Na–Al–O space, which were obtained from the MP[57]. The phase diagram for the Na–Y–Zr–O system in equilibrium with Na metal was constructed based on information from the MP[26]. For the ab initio molecular dynamic simulation (AIMD), a plane wave energy cutoff of 400 eV was chosen and a minimal Γ-centred 1 × 1 × 1 k-point grid was used. All the ab initio molecular dynamic simulations were performed in the NVT (constant number, volume and temperature) ensemble using a Nosé–Hoover thermostat AIMD. The calculated system was constructed with 12 NaFSI, 8 KFSI and 32 MnO$_2$, which corresponds to 296 atoms. The system was heated to 330 K and equilibrated for 10 ps and then simulated for another 10 ps to gather the statistics. The structural matching results were visualized using the VESTA software[58].

The solid Na and YSZ@BASE interfaces were modelled with a Na(110) interacting with the periodic YSZ(111) and BASE(001) substrate surface slabs. The initial configurations of the metal clusters were taken from their crystal bulk structures. The composition of Na$_{30}$Al$_{198}$O$_{306}$ for BASE and Zr$_{17}$Y$_7$O$_{46}$ for YSZ were chosen for the simulation. The adhesion energy is calculated based on the Young–Dupre equation[13,59]. For the Na self-diffusion calculation, the MD simulations were carried out by LAMMPS using the MEAM potential[60] at temperatures from 300 to 380 K. The MD simulations were performed in the NPT ensemble at $P = 1$ atm and $T = 298$ K with a Nose–Hoover barostat and thermostat for 5 ns with a time step of 1.0 fs to integrate the equations of motion. Periodic boundary conditions were used, and electrostatic interactions were considered using the particle–particle particle–mesh scheme in the k space. Subsequently, 10 ns equilibration MD runs were performed in the NVT ensemble, followed by 10 ns NVT production runs that were used to extract the structural properties.

Data availability
All relevant data that support the plots within this article and other findings of this study are available from the corresponding authors upon request.

References
48. Bish, D. L. & Howard, S. Quantitative phase analysis using the Rietveld method. *J. Appl. Crystallogr.* **21**, 86–91 (1988).
49. Cheary, R. W. & Coelho, A. A fundamental parameters approach to X-ray line-profile fitting. *J. Appl. Crystallogr.* **25**, 109–121 (1992).
50. Reed, D. et al. Wetting of sodium on β″-Al$_2$O$_3$/YSZ composites for low temperature planar sodium-metal halide batteries. *J. Power Sources* **227**, 94–100 (2013).
51. Huntington, H. B. Ultrasonic measurements on single crystals. *Phys. Rev.* **72**, 321 (1947).
52. de With, G. & Wagemans, H. H. Ball-on-ring test revisited. *J. Am. Ceram. Soc.* **72**, 1538–1541 (1989).
53. Han, F., Zhu, Y., He, X., Mo, Y. & Wang, C. Electrochemical stability of Li$_{10}$GeP$_2$S$_{12}$ and Li$_7$La$_3$Zr$_2$O$_{12}$ solid electrolytes. *Adv. Energy Mater.* **6**, 1501590 (2016).
54. Kresse, G. & Furthmüller, J. Efficient iterative schemes for ab initio total-energy calculations using a plane-wave basis set. *Phys. Rev. B* **54**, 11169 (1996).
55. Blöchl, P. E. Projector augmented-wave method. *Phys. Rev. B* **50**, 17953 (1994).
56. Perdew, J. P., Ernzerhof, M. & Burke, K. Rationale for mixing exact exchange with density functional approximations. *J. Chem. Phys.* **105**, 9982–9985 (1996).
57. Ong, S. P., Wang, L., Kang, B. & Ceder, G. Li−Fe−P−O$_2$ phase diagram from first principles calculations. *Chem. Mater.* **20**, 1798–1807 (2008).
58. Momma, K. & Izumi, F. VESTA 3 for three-dimensional visualization of crystal, volumetric and morphology data. *J. Appl. Crystallogr.* **44**, 1272–1276 (2011).
59. Young, T. III. An essay on the cohesion of fluid. *Phil. Trans. R. Soc. Lond.* **1805**, 65–87 (1805).
60. Kim, Y., Ko, W.-S. & Lee, B.-J. Second nearest-neighbor modified embedded atom method interatomic potentials for the Na unary and Na–Sn binary systems. *Comp. Mater. Sci.* **185**, 109953 (2020).

Author contributions
T.D., Chunsheng Wang and X.L. proposed the research and designed the experiment. T.D., X.L., O.C., L.C., T.R.A. and H.-J.C. performed the experiments (material synthesis, characterization, battery fabrication and testing, and so on). X.J., T.D., Chungsheng Wang and X.L. conceived the simulation protocol, and X.J. carried out the simulations. L.Z., Chongmin Wang and X.F. performed the TEM, FIB, STEM–EDS analyses. T.D., Chungsheng Wang and X.L. analysed the data and wrote the manuscript with suggestions and comments from all the authors. All the authors contributed to the interpretation of the results.

Competing interests
The authors declare no competing interests.

Additional information
Supplementary information The online version contains supplementary material available at https://doi.org/10.1038/s41565-021-01036-6.

Correspondence and requests for materials should be addressed to Chunsheng Wang or Xiaochuan Lu.

Peer review information *Nature Nanotechnology* thanks Yoon Seok Jung, Guoxiu Wang and the other, anonymous, reviewer(s) for their contribution to the peer review of this work.

Reprints and permissions information is available at www.nature.com/reprints.